Multiobjective component sizing of a hybrid ethanol-electric vehicle propulsion system

He, Y., Wang, C., Zhou, Q., Li, J., Makridis, M., Williams, H., Lu, G. & Xu, H.

Original citation & hyperlink:
He, Y, Wang, C, Zhou, Q, Li, J, Makridis, M, Williams, H, Lu, G & Xu, H 2020, 'Multiobjective component sizing of a hybrid ethanol-electric vehicle propulsion system', Applied Energy, vol. 266, 114843.
https://dx.doi.org/10.1016/j.apenergy.2020.114843

DOI 10.1016/j.apenergy.2020.114843
ISSN 0306-2619

Publisher: Elsevier

Multiobjective component sizing of a hybrid ethanol-electric vehicle propulsion system

Yinglong He[a], Chongming Wang[b], Quan Zhou[a], Ji Li[a], Michail Makridis[c], Huw Williams[a], Guoxiang Lu[a, d, *], Hongming Xu[a,*]

[a]*Mechanical Engineering, the University of Birmingham, Birmingham B15 2TT, United Kingdom*
[b]*Aerospace and Automotive Engineering, Coventry University, Coventry CV1 5FB, United Kingdom*
[c]*Directorate for Energy, Transport and Climate Change, Joint Research Centre, Ispra, Italy*
[d]*BYD Auto Industry Company Limited, Shenzhen, China*

***Abstract*—Concerns over energy efficiency and greenhouse gas (GHG) emissions are driving research investments into advanced propulsion technologies. Plug-in hybrid electric vehicles (PHEVs) can provide a bridge that connects transport electrification to renewable bioenergy sources such as ethanol. However, it remains unclear how this pathway can simultaneously address economic, energy and environmental goals. To tackle this challenge, the present study explores, for the first time, the multiobjective optimal sizing of PHEVs powered by low-carbon sources of electricity and ethanol-gasoline blend. The empirical ethanol-gasoline blend model is incorporated into the PHEV simulation whose relevant parameters are validated using laboratory data from the European Commission – Joint Research Centre. We develop a full picture of the use-phase well-to-wheel (WTW) GHG emissions from ethanol, gasoline and grid electricity and their energy consumptions. Consequently, market-oriented PHEV sizing solutions are provided as per the power utility generation portfolio and automobile fuel properties of the target region. The results indicate that better performances of the PHEV, regarding GHG emissions and energy consumption, are associated with larger battery size and smaller engine displacement but result in a higher cost-to-power ratio. Specifically, for E25-fuelled PHEVs in markets with world average electricity carbon intensity, every 1.0 USD/kW increase in cost-to-power ratio leads to savings of 1.6 MJ energy consumption and 1.7 g CO_2-eq/km WTW GHG emissions. Moreover, a clear benefit of using E25 in the hybrid propulsion system is identified, where the energy consumption and GHG emissions can be reduced by 5.9 % and 12.3 %, respectively.**

***Keywords*—low carbon propulsion, multiobjective optimization, ethanol-gasoline blends, plug-in hybrid electric vehicle.**

I. Introduction

Transport is a major source of greenhouse gas (GHG) emissions and unsustainable energy use due to a nearly complete dependence on liquid fossil fuels [1]. Intensive efforts have been directed at battery and biofuel technologies, which have made electric and flex-fuel vehicles (EVs and FFVs) potentially important strategies to decarbonize transport [2]. However, the market penetration of EVs remains marginal owing to higher cost, increased weight, limited range, and slow charging process [3]. The main barriers to the adoption of FFVs running on ethanol are high cost relating to powertrain enhancements and the potential to pose a big threat to food security [4]. To overcome these limitations, the view from BYD Auto, a Chinese multinational automaker, is that plug-in hybrid electric vehicles (PHEVs) could provide a bridge that connects powertrain electrification to renewable ethanol. The reason for this is the PHEV can use an onboard battery to travel on electricity from the grid, and it can burn liquid fuel, operating as a traditional hybrid electric vehicle (HEV).

Despite the surging acceptance of PHEVs, little progress has been made to simultaneously address economic, energy and environmental goals in the design of PHEVs powered by low-carbon sources of electricity and ethanol. In PHEVs design, the optimal sizing of the key mechanical and electrical components has significant effects on driving performance and cost-effectiveness [5]. Some valuable insights have been reported in the literature [6], [7], being primarily concerned with the optimal sizing of lithium-ion batteries, ultracapacitors, and the internal combustion engine (ICE). For example, Hu et al. [8] presented a battery sizing framework for PHEVs to minimize CO_2 emissions. Wu et al. [9] demonstrated a cost-optimal sizing of drivetrain components including batteries and ICE, etc.

The lithium-ion battery represents the most widely used electric energy storage module because of its high energy densities [10], both gravimetric and volumetric. However, its relatively low power density often results in an oversizing, and thus the excess cost, of the battery pack, in order to deal with high power transients in real-world driving scenarios [11]. Furthermore, increased load frequency is reported to reduce battery durability [12]. Consequently, the role of the ultracapacitor has received considerable critical attention in automotive propulsion systems [13] mainly due to its high power density, fast charge, and wide operational range. In the recent study by Zhang et al. [14], the energy storage system comprising batteries and ultracapacitors is shown to fully exploit the synergistic benefits of these two devices.

To address limitations of the above electric energy storage devices, such as range anxiety and lack of charging infrastructure, the ICE installed in the PHEV can use liquid fuels and act as an onboard charging device [15]. In addition, various techniques have been developed to make ICEs greener, cleaner, and more efficient [16]. Among them, ethanol-gasoline blends have attracted considerable attention from both scholars and the wider community [17]. For example, Wang et al., in their recently published articles [18], [19], have demonstrated clear benefits of ethanol addition for the enhancement of engine

This document is the results of the research project funded by the State Key Laboratory of Automotive Safety and Energy under Project No. KF2029.
* Corresponding authors: Guoxiang Lu (lu.guoxiang@byd.com) and Hongming Xu (h.m.xu@bham.ac.uk).

efficiency and the reduction of emissions. Furthermore, Samaras et al. [20] have stressed that the reduced liquid fuel requirements of PHEVs could utilize limited ethanol resources, without threat to food security. Bradley et al. [21] present the PHEVs design considerations including vehicle component function, energy management systems and energy storage trade-offs. Some studies on PHEVs have shown larger regional GHG reductions in areas with less GHG-intensive generation portfolios [22].

Therefore, the incorporation of multiple targets, including energy consumption, cost-effectiveness, and emissions, is important when approaching the optimal PHEV component sizing. The multiobjective optimization methods can be categorized into the following two broad groups:

1) Weighted-sum methods aggregate multiple objectives into a single cost function that is then minimized [23]. Zhou et al. [5] developed a particle swarm optimization (PSO) algorithm utilized in the optimal PHEV sizing. In this algorithm, the single cost function aims to minimize the overall volume and maximize energy efficiency. The weighted-sum methods cannot, however, determine the weights and the normalization factors that can optimally balance and scale the multiple objective functions for a problem with little or no information [24], which can cause misleading optimization results.
2) Pareto-optimal methods offer a set of Pareto-optimal (or non-dominated) solutions [25], where no single solution is better than another in every criterion [26]. Zhang et al. [14] have employed a non-dominated sorting genetic algorithm (NSGA) to reduce the manufacturing cost of the energy storage system and prolong battery life. The resulting Pareto-optimal set provides the performance boundaries and relationships (e.g., conflicting or harmonious) of the objective functions, therefore, it is an important input to the system design process [27].

Using an advanced Pareto-based optimization algorithm, this work contributes to the multiobjective PHEV component sizing by including several aspects omitted by previous studies. First, an empirical ethanol-gasoline blend model is incorporated into the PHEV simulation. Second, we develop a full picture of the use-phase well-to-wheel (WTW) GHG emissions from ethanol, gasoline and grid electricity and their energy consumptions. Third, market-oriented PHEV design solutions can be provided since the power utility generation portfolio and automobile fuel properties of the target market are considered. Finally, the present work highlights the Pareto relationships among the economic, energy and environmental goals in PHEV design.

The remainder of the paper is organized as follows: Section II presents the ethanol-gasoline blend model. Section III describes the hybrid ethanol-electric propulsion system. Section IV gives the methodology underlying the multiobjective optimization approach where the cost-to-power ratio, the energy consumption, and the GHG emissions are simultaneously minimized. Section V provides the results, followed by the key conclusions summarized in Section VI.

II. Ethanol-gasoline Blend Model

An accurate ethanol-gasoline blend model is vitally important because a precise knowledge of ethanol blends and their influencing factors can be instrumental in the implementation of component sizing and energy management. The authors, in our recently published articles [18], [19], have proposed an empirical ethanol-gasoline blend model based on historical and literature data to evaluated statistical benefits of ethanol use on the engine thermal efficiency gains and WTW GHG emissions. Table 1 lists the main properties of typical gasoline and ethanol used in automotive applications. What is important for us to recognize here, is that although lower in energy density (i.e., lower heating value, H_v), ethanol has a higher research octane number (N_{RON}) that can lead to an increased compression ratio and thence to enhanced engine thermal efficiency. Moreover, the GHG intensity (E_{GHG}) of ethanol is only about one-third of its gasoline counterpart.

Table 1. Fuel properties [18]

Parameter (unit)	Gasoline	Ethanol
N_{RON}, research octane number	89	107
S_O, octane sensitivity	10	18
ρ_f, fuel density(kg/m^3)	730	790
H_v, lower heating value (MJ/kg)	42	26.9
E_{GHG}, WTW GHG emission (g CO_2-eq/MJ)	93.2	33.5

Fig. 1 (a) shows the engine thermal efficiency gain β due to the beneficial effects of ethanol addition. In the literature on ethanol blends, there are three principal effects of ethanol addition on engine hardware design and fuel consumption: 1) anti-knock; 2) high flame speed; 3) engine downsizing. These are factors contributing to total engine thermal efficiency gain β that varies as a function of the ethanol content, described as

$$\beta(\varphi_e) = \beta_{AK}(\varphi_e) + \beta_{FS}(\varphi_e) + \beta_{ED}(\varphi_e), \quad (1)$$

where φ_e is the volumetric content of ethanol (*vol*. %); the subscripts, AK, FS, and ED denote the effects of anti-knock, flame speed, and engine downsizing, respectively. The anti-knock engine efficiency gain can be calculated by

$$\beta_{AK}(\varphi_e) = (k_0\Delta N_{RON} + k_1){\varphi_e}^2 + (k_2\Delta N_{RON} + k_3\Delta S_O + k_4)\varphi_e, \quad (2)$$

where k_0, k_1, k_2, k_3, and k_4 are coefficients derived from the engine tests using ethanol blends, more details are available in [18]; ΔN_{RON} and ΔS_O are differences between ethanol and gasoline, in terms of research octane number and octane sensitivity, respectively, as expressed below.

$$\begin{cases}\Delta N_{RON} = N_{RON}^{ethanol} - N_{RON}^{gasoline}, \\ \Delta S_O = S_O^{ethanol} - S_O^{gasoline}, \end{cases} \quad (3)$$

In addition, the contributions of high flame speed and engine downsizing effects to engine efficiency are quantified as

$$\begin{cases}\beta_{FS}(\varphi_e) = \gamma\varphi_e, \\ \beta_{ED}(\varphi_e) = (\alpha - 1)\big(\beta_{AK}(\varphi_e) + \beta_{FS}(\varphi_e)\big), \end{cases} \quad (4)$$

where γ and α are factors equal to 0.02 and 1.1, respectively.

Furthermore, the ethanol-gasoline blend model provides the estimation of the GHG intensities (g CO_2-eq/MJ) of ethanol blends, which can be linearly calculated by

$$E_{GHG}^{fuel}(\varphi_e) = b_0 + b_1\varphi_e, \quad (5)$$

where b_0 and b_1 are constant coefficients determined by the gasoline and ethanol properties. As shown in Fig. 1 (b), with successive increases in ethanol content φ_e from 0 to 25, the GHG intensity of the fuel blend is decreased from 93.2 to 81.8 g CO_2-eq/MJ, indicating significant reductions in total GHG emission (~12 %, from blend) and in fossil GHG emission (~20 %, from gasoline).

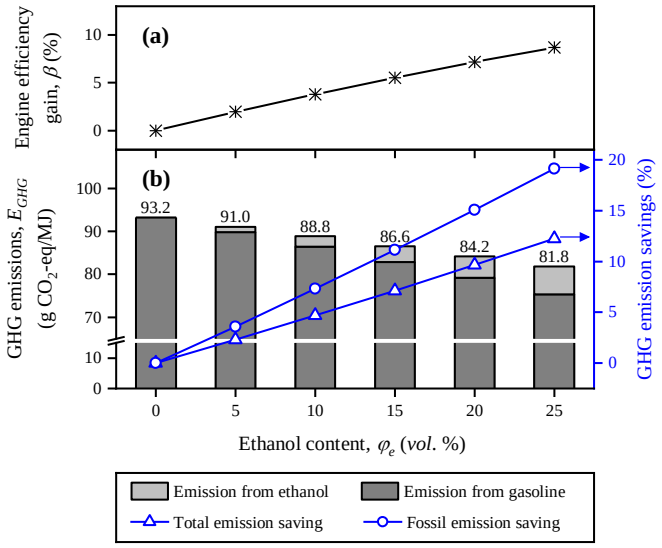

Fig. 1. The energy and emission benefits of different ethanol-gasoline blends. (a) Engine efficiency gain. (b) GHG emissions.

The ethanol-gasoline blend model can be applied for up to 70 *vol*. % ethanol blends [18]. However, the blend whose ethanol content is beyond 25 *vol*. % cannot be used in regular engines [28], causing high cost relating to engine enhancements. Therefore, the ethanol content (φ_e) in blends ranges between 0 and 25 in this study.

III. Hybrid Ethanol-Electric Propulsion System

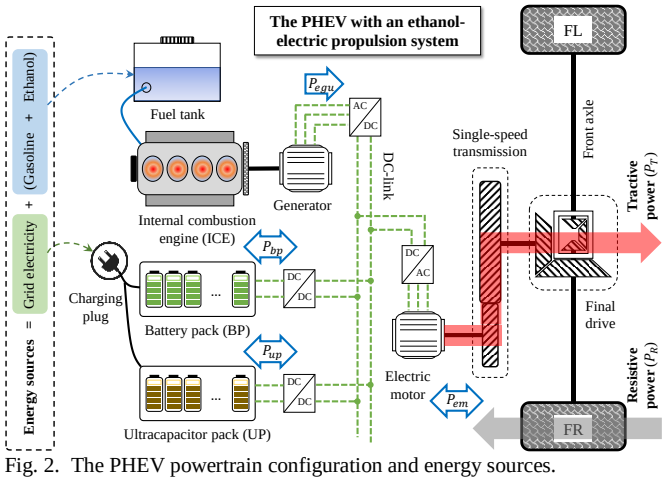

Fig. 2. The PHEV powertrain configuration and energy sources.

As illustrated in Fig. 2, the PHEV propulsion system examined here comprises a set of mechanical and electrical components. The battery pack (BP) and the ultracapacitor pack (UP) can both store grid electricity. The ICE that is connected to the liquid fuel tank and the generator can use chemical energy obtained from the ethanol-gasoline blend to charge the batteries and ultracapacitors when their grid electricity is depleted or to propel the wheels via the electric motor. In addition, the kinetic energy harvested by regenerative braking can also be stored in the BP and the UP. The involved energy conversion and management processes are introduced below.

A. Vehicle Dynamics

The vehicle longitudinal dynamics can be described by

$$\begin{cases} v(t) = \dot{d}(t), \\ a(t) = \dfrac{1}{\delta m}\big(F_T(t) - F_R(t)\big), \\ F_T(t) = \dfrac{1000 P_{em}(t)\eta_d}{v(t)}, \\ F_R(t) = f_2 v(t)^2 + f_1 v(t) + f_0 \cos\theta + mg\sin\theta, \end{cases} \tag{6}$$

where a, v and d are acceleration (m/s^2), speed (m/s), and travel distance (m), respectively, of the subject vehicle at time t (s); m is the vehicle operating mass (kg); δ is the equivalent inertial mass; P_{em} denotes the power (kW) of the electric motor; η_d is the driveline efficiency; F_T is the tractive forces; F_R indicates the resistance forces acting on the vehicle, namely, the aerodynamic, rolling and grade resistance; f_0, f_1, and f_2 are the road load coefficients [29]; and θ is the road grade (rad).

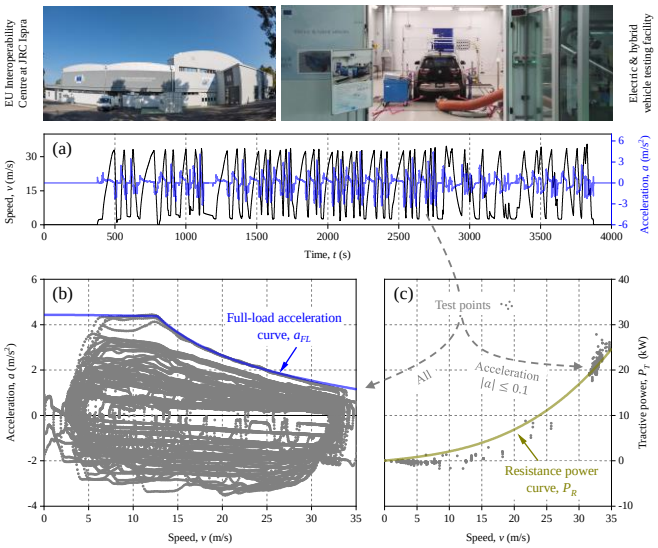

Fig. 3. The validation of the vehicle dynamics model in laboratories. (a) Test cycles. (b) Validation of theoretical full-load acceleration. (c) Validation of theoretical resistance power.

As presented in Fig. 3, the vehicle dynamics are validated using chassis dynamometer tests carried out in laboratories of the European Commission – Joint Research Centre (JRC). Fig. 3 (a) shows 46 consecutive test cycles with different acceleration and deceleration rates. Fig. 3 (b) compares measured data points with the theoretical full-load acceleration curve a_{FL} derived from equation (6). It is worth noting that there are few data points at low-speed (less than ~5 m/s) region because the speed range for these tests is between 20 and 120 km/h. It is apparent that the theoretical a_{FL} curve demonstrates a good correlation with the upper boundary test points. Fig. 3 (c) selects test points with small accelerations (i.e., $|a| \leq 0.1$), so that their tractive power P_T is approximately equal to their resistance power P_R. The observed strong correlation between the theoretical P_R curve and measured P_T points further supports the robustness and reliability of the vehicle dynamics model used in this work.

B. Internal Combustion Engine

An empirical 1.0 L engine model from the AVL CRUISE software was selected as the baseline for the component sizing. It is assumed that the engine operation points always lie on the highest efficiency curve across the entire power range of the engine, which is normalized against its maximum power (40 kW) [30]. According to Willans method adopted by Zhou et al. [5] and Lujan [31], the maximum power of the engine can be scaled by considering its displacement, and thus, its instantaneous fuel consumption rate ($\dot{m}$) can be estimated by

$$\begin{cases} \dot{m}(t) = \dfrac{P_{ice}(t)}{H_v(\varphi_e)\cdot\left(1+\beta(\varphi_e)\right)\cdot\eta_{ice}^{base}(P_{ice}^{n})}, \\ P_{ice}^{n} = \dfrac{P_{ice}(t)}{P_{ice}^{max}}, \\ P_{ice}^{max}(V_{ice}) = k_s V_{ice}\,, \end{cases} \tag{7}$$

where P_{ice}^{max} is the maximum engine power (kW); V_{ice} indicates the engine displacement (L); k_s is the engine scale factor; $\dot{m}$ is the fuel consumption rate (g/s); P_{ice} is the current engine power output (kW); P_{ice}^{n} is a dimensionless quantity and denotes the normalized engine power; η_{ice}^{base} is the baseline engine efficiency function illustrated in Fig. 4; H_v is the lower heating value (MJ/kg) of the fuel blend. The cost estimation method for a regular engine, adopted by Wu et al. [9], is expressed as

$$c_{ice}(V_{ice}) = 12P_{ice}^{max}(V_{ice}) + 424, \tag{8}$$

where c_{ice} is the cost (USD) of the engine whose maximum power is P_{ice}^{max}.

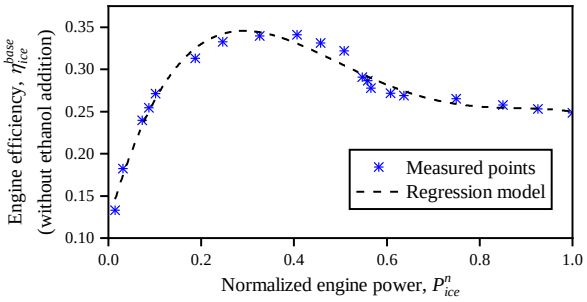

Fig. 4. The efficiency curve of the baseline engine fueled with gasoline (without ethanol addition).

C. Battery and Ultracapacitor

Table 2. Main specifications of the battery and the ultracapacitor [5], [14]

Parameter (unit)	Value
Battery cell	
m_{bc}, mass (g)	46.5
V_{bc}, nominal voltage (V)	3.6
Q_{bc}, energy capacity (As)	11500
R_{bc}, resistance (Ω)	0.01
c_{bc}, cost (USD)	6.5
Ultracapacitor cell	
m_{uc}, mass (g)	535
V_{uc}, nominal voltage (V)	2.7
Q_{uc}, energy capacity (As)	4000
C_{uc}, capacitance (F)	3000
c_{uc}, cost (USD)	32.5

The battery pack (BP) and ultracapacitor pack (UP) are scaled by their cell numbers, namely, n_{bc} and n_{uc}, respectively. Taken from the study by Zhou et al. [5], the types of lithium-ion battery and ultracapacitor are Panasonic NCR18650BF and NessCap ESHSR-3000C0-002R7A5T, respectively, whose main specifications are summarized in Table 2. The battery physics is simulated by the model proposed by Chen et al. [32], while the mathematical model adopted for the ultracapacitor simulation is based on the study by Ostadi et al. [6]. To avoid the detrimental effects of overcharge and overdischarge, the operating window of battery state-of-charge (SoC) is from 0.2 to 0.8; while for ultracapacitor, its SoC is bounded between 0.2 to 0.9, following Zhang et al. [14].

D. Energy Management Strategy

Torque/power coordination is essential for realizing PHEVs' low-carbon and high-efficiency potentials [33]. Thus, the hybrid propulsion system needs capable energy management strategies (EMSs) to coordinate the power outputs from the engine-generator unit (EGU), battery pack (BP), and ultracapacitor pack (UP). In this work, two widely-used EMSs including CD-CS (charge depleting – charge sustaining) and WT (wavelet transform) are employed to realize the power split among EGU, BP, and UP.

The overall power-balance equations are

$$\begin{cases} \dfrac{P_{em}(t)}{\eta_{em}{\eta_i}^2} = P_{ice}(t)\eta_g + P_{ele}(t), \\ P_{ele}(t) = P_{bp}(t) + P_{up}(t), \end{cases} \tag{9}$$

where η_{em} is the motor efficiency; η_i indicates the inverter efficiency; η_g is the generator efficiency; P_{ele} is the power (kW) delivered from the electricity storage components; and P_{bp} and P_{up} are the power outputs (kW) of the battery pack and the ultracapacitor pack, respectively.

The CD-CS technique [34] is applied to split the mechanical (P_{ice}) and electrical (P_{ele}) power outputs, where the former varies as a stepwise function of the battery SoC.

$$P_{ice}(t) = \begin{cases} 0, & SoC_{bc} \in (0.8, 1] \\ \dfrac{round\left(20e^{-\frac{(SoC_{bc}(t)-0.2)^2}{2\sigma^2}}\right)}{20} P_{ice}^{max}, & SoC_{bc} \in [0.2, 0.8] \\ P_{ice}^{max}, & SoC_{bc} \in [0, 0.2) \end{cases} \tag{10}$$

where σ is the time constant; SoC_{bc} is the battery state-of-charge (SoC). The battery dynamics [35], [36] are governed by the following equations.

$$\begin{cases} P_{bc}(t) = \dfrac{P_{bp}}{n_{bc}} = V_{bc}I_{bc} - {I_{bc}}^2 R_{bc}, \\ \dot{SoC}_{bc}(t) = -\dfrac{I_{bc}}{Q_{bc}} = -\dfrac{V_{bc} - \sqrt{{V_{bc}}^2 - 4R_{bc}P_{bc}(t)}}{2R_{bc}Q_{bc}}, \end{cases} \tag{11}$$

where P_{bc} and I_{bc} are respectively the power (W) and the current (A) of the battery cell; R_{bc}, Q_{bc}, and V_{bc} denote the internal resistance (Ω), energy capacity (As), and open-circuit voltage (V), respectively; n_{bc} is the cell number in the battery pack.

In addition, the WT technique uses high-pass and low-pass filters to decompose the electrical power signal (P_{ele}) into different localized contributions, each of which represents a portion of the signal from a different frequency band [37]. Consequently, the high frequency components are dealt with by

the highly responsive ultracapacitor pack (UP); while the remaining parts are consigned to the battery pack (BP). This approach, as expressed in the following equations, can help to protect battery cells from too much transient charging and discharging.

$$\begin{cases} P_{bp}(t) = f_{low-pass}\big(P_{ele}(t)\big), \\ P_{up}(t) = f_{high-pass}\big(P_{ele}(t)\big), \end{cases} \tag{12}$$

IV. Optimization Methodology

The working principle of the multiobjective optimal sizing conducted in this study is illustrated in Fig. 5. The input layer, as presented in Fig. 5 (a), provides information from the real-world measurements, standards, and requirements, for the formulation of the multiobjective optimization problem (MOP). The driving cycle used is three consecutive repetitions of the worldwide harmonized light vehicle test cycle (3×WLTC). The vehicle resistance factors are validated with chassis dynamometer tests shown in Fig. 3. As mentioned in the previous section, the ethanol and gasoline properties are fed into the fuel blend model for the estimation of engine efficiency and GHG emission. The optimization layer, given in Fig. 5 (b), is the flow chart of the non-dominated sorting genetic algorithm III (NSGA-III) employed to solve the formulated MOP. The output layer, presented in Fig. 5 (c), utilizes the desirability function to derive the best compromise solution from the Pareto frontier resulting from the NSGA-III optimization.

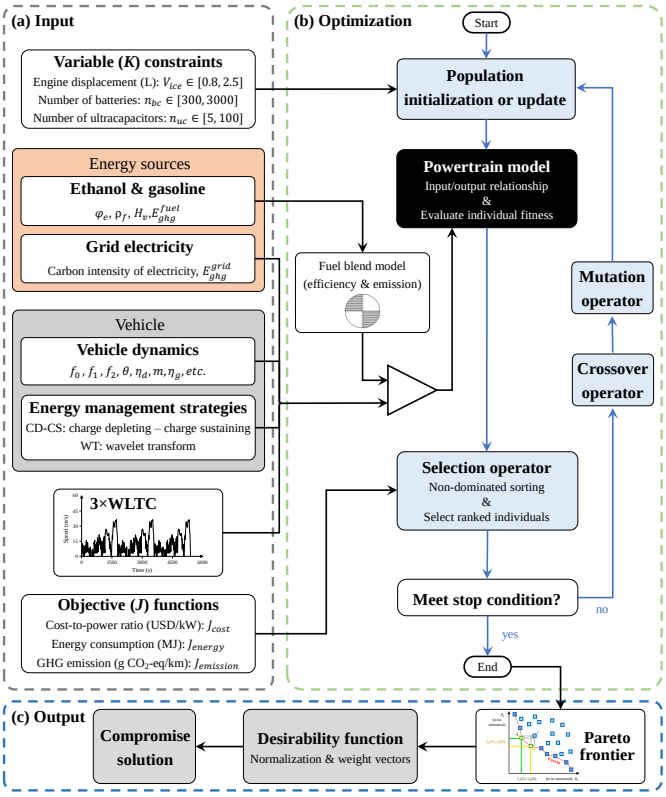

Fig. 5. Working principle of the multiobjective optimal sizing: (a) the input layer including the real-world measurements, standards, and requirements; (b) the optimization layer implementing the Pareto-based NSGA-III algorithm; (c) the output layer utilizing the desirability function to derive the best compromise solution from the Pareto frontier.

A. Optimal Sizing Problem Formulation

The primary goal of this study is to investigate the optimal sizing, i.e., the engine displacement (V_{ice}), the number of batteries (n_{bc}), and the number of ultracapacitors (n_{uc}), of the PHEV using multiple energy streams. To this end, three objective functions, namely cost-to-power ratio (J_{cost}), energy consumption (J_{energy}), and GHG emission ($J_{emission}$) are defined as follows to encompass economic, efficiency, and environmental needs.

The cost-to-power ratio (USD/kW) is the value of the components' total manufacturing cost divided by the maximum power that the propulsion system can deliver. Its mathematical expression is given below.

$$\begin{cases} J_{cost} = \dfrac{c_{ice}(V_{ice}) + c_{bc}n_{bc} + c_{uc}n_{uc}}{P_{ice}^{max}(V_{ice}) + \varepsilon_{bp}P_{bc}^{max}n_{bc} + \varepsilon_{up}P_{uc}^{max}n_{uc}}, \\ \varepsilon_{bp} = \dfrac{n_{bc}Q_{bc}}{n_{bc}Q_{bc} + n_{uc}Q_{uc}}, \\ \varepsilon_{up} = \dfrac{n_{uc}Q_{uc}}{n_{bc}Q_{bc} + n_{uc}Q_{uc}}, \end{cases} \tag{13}$$

where P_{bc}^{max} and P_{uc}^{max} are the maximum power outputs (kW) of the battery cell and the ultracapacitor cell, respectively. As mentioned in the literature review, the ultracapacitor has a high power density but has a much lower energy density when compared with the battery. Considering that the sustainability of their maximum power outputs is limited by the energy available in these two devices, the power adjustment factors ε_{bp} and ε_{up} are incorporated into the cost function.

The energy consumption (MJ) includes the consumed ethanol-gasoline blend and grid electricity during the 3×WLTC test cycle. The expressions are presented as follows.

$$\begin{cases} J_{energy} = \displaystyle\int_{t_0}^{t_f} \frac{H_v(\varphi_e)\dot{m}(t) + P_{bp}(t) + P_{up}(t)}{1000}\,dt, \\ P_{bp}(t) = n_{bc}P_{bc}(t), \\ P_{up}(t) = n_{uc}P_{uc}(t), \end{cases} \tag{14}$$

where t_0 and t_f represent the initial time and final time of the driving cycle.

Life cycle assessment (LCA) is a standardized tool to quantify GHG emissions associated with a product's manufacture, use, and end-of-life [20]. In this paper, the use-phase well-to-wheel (WTW) GHG emission (g CO_2-eq/km), resulting from powering the vehicle with liquid fuel and grid electricity [38], is given below.

$$J_{emission} = \frac{1}{d}\int_{t_0}^{t_f}\Big(E_{ghg}^{fuel}(\varphi_e)H_v(\varphi_e)\dot{m}(t) + E_{ghg}^{grid}\Big(P_{bp}(t) + P_{up}(t)\Big)\Big)\,dt, \tag{15}$$

where E_{ghg}^{grid} is the carbon intensity (g CO_2-eq/MJ) of the grid electricity stored in batteries and ultracapacitors. As reported by the International Energy Agency (IEA) [39], for the base-case scenario, grid electricity used to charge PHEVs has the WTW GHG intensity E_{ghg}^{grid} similar to the average intensity of the current world power portfolio, or 146.9 g CO_2-eq per MJ of electricity.

Moreover, according to a dataset of vehicle specifications that contains information relating to 543 commercial hybrid

electric vehicles, the multiobjective optimization is subject to the following constraints on the controlled variables.

$$\begin{cases} 0.8\,L \le V_{ice} \le 2.5\,L \\ 0 \le n_{uc} \le 100 \\ 300 \le n_{bc} \le 3000 \end{cases} \quad (16)$$

B. Optimization Using Pareto Genetic Algorithm

NSGA-III has been recognized to be an effective and efficient algorithm to solve multiobjective optimization problems (MOPs) [40]–[42], where an approximation of the Pareto-optimal set can be obtained in a single run. The flow chart of the NSGA-III optimization in this study is illustrated in Fig. 5 (b). The vector of controlled variables is expressed as a chromosome where each variable is the gene. There are three fundamental genetic operators: 1) the crossover operator exchanges the gene information of the current generation, in order to share the better gene segment; 2) the mutation operator then randomly alters some genes of the chromosome to perform a local search, attempting to find a better fitness landscape; 3) the selection operator finally determines the survived population for the next generation.

C. Desirability Function

In engineering applications, usually only one PHEV design solution is required, thus, the desirability function is introduced to select the best compromise solution from the Pareto frontier, as shown in Fig. 5 (c). The method adopted by Pasandideh et al. [43] computes a penalty score α for each objective vector in the Pareto-optimal set. Consequently, the solution with the minimum α is the best compromise one. The expressions of the desirability function are presented as follows.

$$\min_{K\in PF} \alpha\big(J(K)\big) = \min_{K\in PF} \sum_{i=1}^{3} w_i \frac{J_i(K)-J_i^{min}}{J_i^{max}-J_i^{min}}, \quad (17)$$

$$\begin{cases} J = [J_{cost}, J_{energy}, J_{emission}], \\ K = [V_{ice}, n_{uc}, n_{bc}], \\ \sum_{i=1}^{3} w_i = 1 \text{ and } w_i \ge 0, \end{cases} \quad (18)$$

where J_i^{max} and J_i^{min} are the maximum and minimum values of the objective function J_i on the Pareto frontier (PF); K is the variable vector; w_i means the weight factor given by the decision-maker.

V. Results and Discussion

The results obtained from the multiobjective component sizing are presented and discussed in the section below from three perspectives: 1) the Pareto analysis seeks to elicit relationships (e.g., conflicting and harmonious) between different objective functions, and thus to provide guidance for the selection of the weight vector w in the desirability function; 2) the performance analysis demonstrates the reliability of the best compromise solution when implemented in the PHEV propulsion system; and 3) the analysis of energy and GHG emission benefits from the ethanol use is presented.

A. Pareto Analysis

Fig. 6 (a) presents the Pareto-optimal set achieved by NSGA-III optimization when φ_e is equal to 25 %. For visualization and analysis purposes, the three-dimensional (3D) objective space is projected onto the 2D scatter plots, i.e., Fig. 6 (b) - (d), where the ideal point (black square, z^{ideal}) and the nadir point (black triangle, z^{nadir}) correspond to the lower and upper boundaries of the Pareto performance range (PPR). The relationships among different objective functions are analyzed as below.

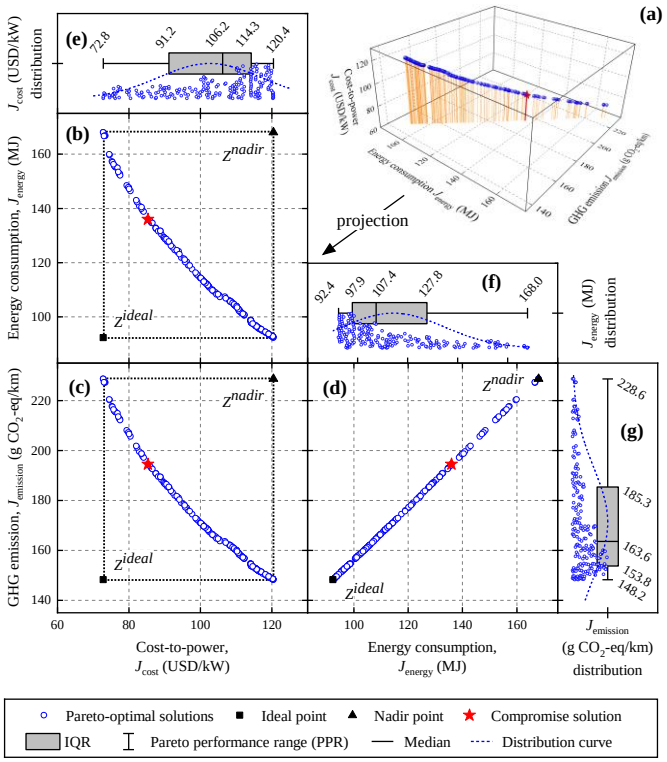

Fig. 6. The Pareto frontier (PF) resulting from the multiobjective optimization. (a) PF in 3D space. (b)-(d) Projections onto 2D planes. (e)-(g) Marginal distributions.

Intuitively with the projection in Fig. 6 (b), a trade-off (or conflicting relationship) can be identified between the manufacturing cost (J_{cost}) and the energy consumption (J_{energy}) targets, because one of them will deteriorate when the other is improved in the Pareto-optimal set. Moreover, there exists a similar trade-off between the cost (J_{cost}) and the emission ($J_{emission}$) targets, as shown in Fig. 6 (c). However, looking at Fig. 6 (d), the optimization of J_{energy} is in harmony with that of $J_{emission}$, where the reduction of any one is rewarded with a simultaneous decrease in the other.

According to relationships of objective functions mentioned above, the weight vector is assigned as w = [0.50, 0.25, 0.25] in this work, because the energy and the emission targets are both in conflict with the cost objective. After the implementation of the desirability function, the best compromise solution is obtained and identified as a pentagram symbol in Fig. 6.

Table 3. Distribution of each objective on the Pareto frontier

Objective	PPR	Median
cost-to-power ratio, J_{cost} (USD/kW)	47.6	106.2
energy consumption, J_{energy} (MJ)	75.6	107.4
GHG emission, $J_{emission}$ (g CO_2-eq/km)	80.4	163.6

The box-whisker diagrams shown in Fig. 6 (e) – (g) provide the statistical distributions of the Pareto-optimal set regarding

each objective. The height of the box is the interquartile range (IQR) between the first quartile (Q_1, 25 %) and the third quartile (Q_3, 75 %). The median, the band inside the box, denotes the second quartile (Q_2, 50 %). The ends of the whisker represent the Pareto performance range (PPR), namely, the range between the ideal point and the nadir point in every objective dimension. As summarized in Table 3, the cost (J_{cost}), energy (J_{energy}), and emission ($J_{emission}$) objectives have a median value of 106.2 USD/kW, 107.4 MJ, and 163.6 g CO_2-eq/km, respectively, in the Pareto-optimal set. More importantly, the PPR data from this table indicates that, for the design of PHEVs fueled with E25, every 1.0 USD/kW increase in cost-to-power ratio leads to savings of 1.6 MJ energy consumption and 1.7 g CO_2-eq/km WTW GHG emission.

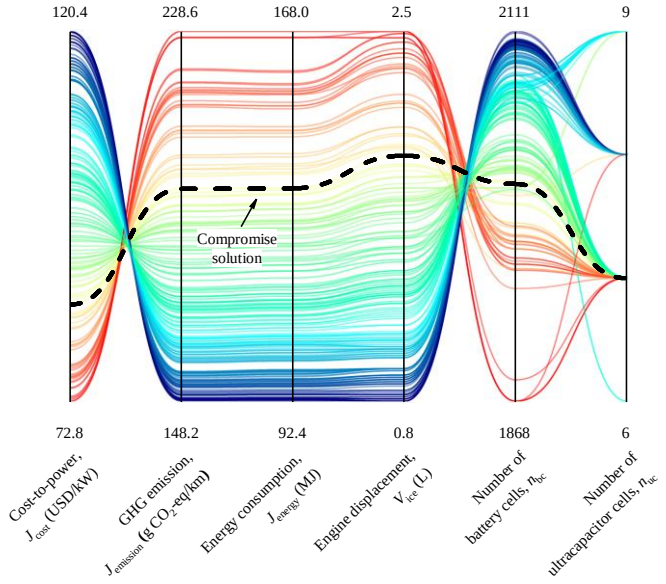

Fig. 7. Parallel coordinates of the Pareto-optimal solutions.

Fig. 7 displays the parallel coordinates, which offer more details in correlating the controlled variables (V_{ice}, n_{bc}, and n_{uc}) with the design objectives (J_{cost}, J_{energy}, and $J_{emission}$). Each dimension is visualized on a vertical axis and each Pareto-optimal solution is presented as a curve connecting the respective values on the vertical axis. In addition, the black dash curve denotes the compromise solution, which is consistent with the preference expressed by the weight vector w. The findings in the parallel coordinates further indicate that better performances of the PHEV propulsion system with respect to GHG emissions and energy consumption are associated with larger battery size and smaller engine displacement, which, conversely, result in a higher cost-to-power ratio.

B. *Performance Analysis*

Fig. 8 demonstrates the performances of the PHEV propulsion system after the implementation of the compromise solution discussed above. Fig. 8 (a) – (c) show the power profiles of the battery pack (BP), the ultracapacitor pack (UP), and the engine-generator unit (EGU). To compare their power transients, two gray sections (time intervals 800 – 1000 s and 4900 – 5100 s) are zoomed in and put into the same power vs time coordinates, as shown in Fig. 8 (e) and (f). The above figures reveal that power coordination among different mechanical and electrical propulsion components can be achieved by the employed CD-CS and WT energy management strategies. The battery pack has a smooth power profile together with reduced power levels, while the ultracapacitor pack assists to share the dynamic transients during the aggressive accelerations and decelerations. The engine-generator unit starts to work at ~3000 s and operates constantly in high-efficiency and low-emission areas since the hybrid powertrain has multiple power sources and makes it easy to adjust the engine operation points [44]. Fig. 8 (d) illustrates the battery SoC and ultracapacitor SoC profiles during the 3×WLTC test cycle, where detrimental overcharge and overdischarge are avoided.

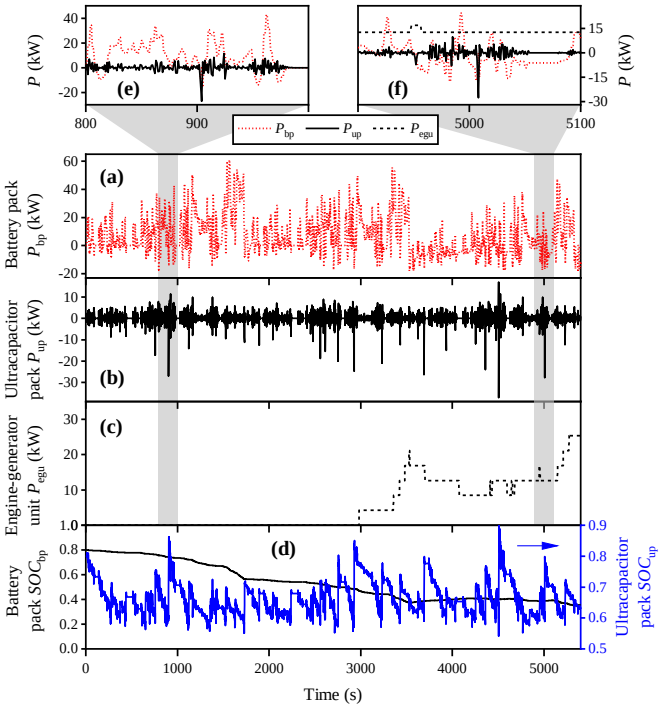

Fig. 8. The power coordination and the performances of components. (a) BP power. (b) UP power. (c) EGU power. (d) SoC.

C. *Analysis of Energy and Emission Benefits*

To analyze the impact of ethanol use on the performance of the optimized PHEV, Fig. 9 compares the cumulative energy consumption and GHG emission for E0 (without ethanol addition, i.e., ethanol content φ_e = 0 %,) and E25 (φ_e = 25 %) scenarios.

Fig. 9 (a) and (b) present results from the simulation of the E0 scenario. It can be seen that the energy consumption and the GHG emission from 3×WLTC cycle are ~145 MJ and ~15.6 kg CO_2-eq, respectively, where the gasoline accounts for 73.7 % of the total energy consumed and 64.0 % of the overall GHG emission. When using the low-carbon E25 fuel blend, an overview of the PHEV energy consumption is displayed in Fig. 9 (c), where the saving of the total energy consumption is 5.95 %, while the corresponding contribution from gasoline is reduced to 58.3 %. Moreover, the emission benefit from ethanol use is provided in Fig. 9 (d), where the saving of total GHG emission is 12.3 %, and the percentage of fossil GHG emission

is reduced to 54.3 %. What is interesting about the data in Fig. 9 (c) and (d) is that ethanol only contributes to 4.6 % of the total GHG emissions although it provides 13.8 % of the total energy.

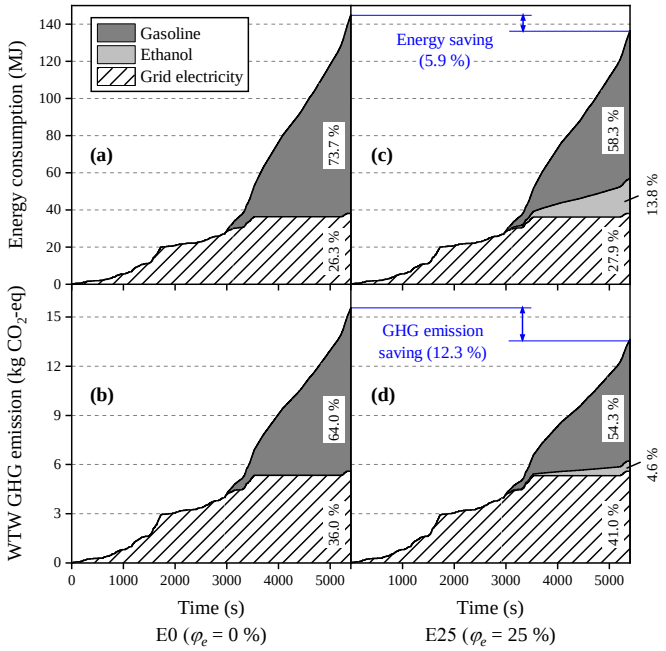

Fig. 9. Energy and emission benefits from ethanol use. (a)-(b) E0-fuelled PHEV. (c)-(d) E25-fuelled PHEV.

VI. Conclusions

To combat climate change and enhance energy security, plug-in hybrid electric vehicles (PHEVs) can provide a bridge that connects transport electrification to renewable ethanol. However, little progress has been made to simultaneously address economic, energy and environmental goals in the design of PHEVs powered by low-carbon sources of electricity and ethanol. This study has thoroughly examined the synergistic benefits of both electric and ethanol low-carbon propulsion techniques within the framework of multiobjective PHEV component sizing. The cost-to-power ratio, energy consumption, and use-phase WTW GHG emission are selected as optimization objectives. The major contribution and conclusions of this paper are as follows:

1. An empirical ethanol-gasoline blend model is incorporated into the PHEV powertrain simulation. Then we develop a full picture of the use-phase WTW GHG emissions from ethanol, gasoline and grid electricity and their energy consumptions.

2. The proposed PHEV component sizing approach can provide market-oriented PHEV design solutions targeted on the power utility generation portfolio and the automobile fuel properties of the market region.

3. Specifically, for E25-fuelled PHEVs in markets with world average (146.9 g CO_2-eq/MJ) electricity carbon intensity, every 1.0 USD/kW increase in cost-to-power ratio leads to savings of 1.6 MJ energy consumption and 1.7 g CO_2-eq/km WTW GHG emissions.

4. A clear benefit of using E25 in the hybrid propulsion system is identified, where the energy consumption and the GHG emissions can be reduced by 5.9 % and 12.3 %, respectively.

5. A moderate proportion of ethanol using E25 in the PHEV can contribute to 13.8 % of the total energy used but counts only 4.8 % of the GHG emissions.

Acknowledgment

This work is based on the collaboration between the University of Birmingham and the Joint Research Centre (JRC) of the European Commission. The authors are grateful to Biagio Ciuffo, Georgios Fontaras, and Konstantinos Mattas of JRC for their advice and support. The authors acknowledge the support of the EPSRC funded project (New Control Methodology for the Next Generation of Engine Management Systems, EP/J00930X/1) and the Innovate UK funded project (Hybrid Electric Push-Back Tractor, 102253).

References

[1] M. Tran, D. Banister, J. D. K. Bishop, and M. D. McCulloch, 'Realizing the electric-vehicle revolution', *Nature Climate Change*, vol. 2, no. 5, pp. 328–333, 2012.

[2] J. E. Campbell, D. B. Lobell, and C. B. Field, 'Greater transportation energy and GHG offsets from bioelectricity than ethanol', *Science*, vol. 324, no. 5930, pp. 1055–1057, 2009.

[3] L. Kumar and S. Jain, 'Electric propulsion system for electric vehicular technology: A review', *Renewable and Sustainable Energy Reviews*, vol. 29, pp. 924–940, 2014.

[4] E. Sadeghinezhad *et al.*, 'A comprehensive literature review of bio-fuel performance in internal combustion engine and relevant costs involvement', *Renewable and Sustainable Energy Reviews*, vol. 30, pp. 29–44, 2014.

[5] Q. Zhou, W. Zhang, S. Cash, O. Olatunbosun, H. Xu, and G. Lu, 'Intelligent sizing of a series hybrid electric power-train system based on chaos-enhanced accelerated particle swarm optimization', *Applied Energy*, vol. 189, pp. 588–601, 2017.

[6] A. Ostadi and M. Kazerani, 'A comparative analysis of optimal sizing of battery-only, ultracapacitor-only, and battery–ultracapacitor hybrid energy storage systems for a city bus', *IEEE Transactions on Vehicular Technology*, vol. 64, no. 10, pp. 4449–4460, 2015.

[7] L. Xu, C. D. Mueller, J. Li, M. Ouyang, and Z. Hu, 'Multi-objective component sizing based on optimal energy management strategy of fuel cell electric vehicles', *Applied Energy*, vol. 157, pp. 664–674, 2015.

[8] X. Hu, S. J. Moura, N. Murgovski, B. Egardt, and D. Cao, 'Integrated optimization of battery sizing, charging, and power management in plug-in hybrid electric vehicles', *IEEE Transactions on Control Systems Technology*, vol. 24, no. 3, pp. 1036–1043, 2016.

[9] X. Wu, B. Cao, X. Li, J. Xu, and X. Ren, 'Component sizing optimization of plug-in hybrid electric vehicles', *Applied Energy*, vol. 88, no. 3, pp. 799–804, 2011.

[10] Y. Zou, S. E. Li, B. Shao, and B. Wang, 'State-space model with non-integer order derivatives for lithium-ion battery', *Applied Energy*, vol. 161, pp. 330–336, 2016.

[11] A. Khaligh and Z. Li, 'Battery, ultracapacitor, fuel cell, and hybrid energy storage systems for electric, hybrid electric, fuel cell, and plug-in hybrid electric vehicles: State of the art', *IEEE Transactions on Vehicular Technology*, vol. 59, no. 6, pp. 2806–2814, 2010.

[12] M. Jafari, A. Gauchia, K. Zhang, and L. Gauchia, 'Simulation and analysis of the effect of real-world driving styles in an EV battery performance and aging', *IEEE Transactions on Transportation Electrification*, vol. 1, no. 4, pp. 391–401, 2015.

[13] L. Zhang, X. Hu, Z. Wang, F. Sun, and D. G. Dorrell, 'Experimental impedance investigation of an ultracapacitor at different conditions for electric vehicle applications', *Journal of Power Sources*, vol. 287, pp. 129–138, 2015.

[14] L. Zhang, X. Hu, Z. Wang, F. Sun, J. Deng, and D. G. Dorrell, 'Multiobjective optimal sizing of hybrid energy storage system for electric vehicles', *IEEE Transactions on Vehicular Technology*, vol. 67, no. 2, pp. 1027–1035, 2018.

[15] J. Li, Q. Zhou, Y. He, H. Williams, and H. Xu, 'Driver-identified supervisory control system of hybrid electric vehicles based on spectrum-guided fuzzy feature extraction', *IEEE Transactions on Fuzzy Systems*, 2020.

[16] C. Wang, A. Janssen, A. Prakash, R. Cracknell, and H. Xu, 'Splash blended ethanol in a spark ignition engine – Effect of RON, octane sensitivity and charge cooling', *Fuel*, vol. 196, pp. 21–31, 2017.

[17] P. Iodice, A. Senatore, G. Langella, and A. Amoresano, 'Effect of ethanol–gasoline blends on CO and HC emissions in last generation SI engines within the cold-start transient: An experimental investigation', *Applied Energy*, vol. 179, pp. 182–190, 2016.

[18] C. Wang, J. M. Herreros, C. Jiang, A. Sahu, and H. Xu, 'Engine thermal efficiency gain and well-to-wheel greenhouse gas savings when using bioethanol as a gasoline-blending component in future spark-ignition engines: A China case study', *Energy & Fuels*, vol. 32, no. 2, pp. 1724–1732, 2018.

[19] C. Wang, S. Zeraati-Rezaei, L. Xiang, and H. Xu, 'Ethanol blends in spark ignition engines: RON, octane-added value, cooling effect, compression ratio, and potential engine efficiency gain', *Applied Energy*, vol. 191, pp. 603–619, 2017.

[20] C. Samaras and K. Meisterling, 'Life cycle assessment of greenhouse gas emissions from plug-in hybrid vehicles: implications for policy', *Environmental Science & Technology*, vol. 42, no. 9, pp. 3170–3176, 2008.

[21] T. H. Bradley and A. A. Frank, 'Design, demonstrations and sustainability impact assessments for plug-in hybrid electric vehicles', *Renewable and Sustainable Energy Reviews*, vol. 13, no. 1, pp. 115–128, 2009.

[22] C. H. Stephan and J. Sullivan, 'Environmental and energy implications of plug-in hybrid-electric vehicles', *Environmental science & technology*, vol. 42, no. 4, pp. 1185–1190, 2008.

[23] X. Hu, J. Jiang, B. Egardt, and D. Cao, 'Advanced power-source integration in hybrid electric vehicles: Multicriteria optimization approach', *IEEE Transactions on Industrial Electronics*, vol. 62, no. 12, pp. 7847–7858, 2015.

[24] M. Awad and R. Khanna, 'Multiobjective optimization', in *Efficient Learning Machines: Theories, Concepts, and Applications for Engineers and System Designers*, Berkeley, CA: Apress, 2015, pp. 185–208.

[25] W. H. van Willigen, E. Haasdijk, and L. J. Kester, 'Evolving intelligent vehicle control using multi-objective neat', in *IEEE Symposium on Computational Intelligence in Vehicles and Transportation Systems (CIVTS)*, 2013.

[26] W. Jakob and C. Blume, 'Pareto optimization or cascaded weighted sum: A comparison of concepts', *Algorithms*, vol. 7, no. 1, pp. 166–185, 2014.

[27] Y. He *et al.*, 'Multiobjective co-optimization of cooperative adaptive cruise control and energy management strategy for PHEVs', *IEEE Transactions on Transportation Electrification*, 2020.

[28] 'Common ethanol fuel mixtures', *Wikipedia*. .

[29] G. Fontaras, N.-G. Zacharof, and B. Ciuffo, 'Fuel consumption and CO2 emissions from passenger cars in Europe–Laboratory versus real-world emissions', *Progress in Energy and Combustion Science*, vol. 60, pp. 97–131, 2017.

[30] K. Yu *et al.*, 'Model predictive control for hybrid electric vehicle platooning using slope information', *IEEE Transactions on Intelligent Transportation Systems*, vol. 17, no. 7, pp. 1894–1909, 2016.

[31] J. M. Luján, C. Guardiola, B. Pla, and A. Reig, 'Cost of ownership-efficient hybrid electric vehicle powertrain sizing for multi-scenario driving cycles', *Proceedings of the Institution of Mechanical Engineers, Part D: Journal of Automobile Engineering*, vol. 230, no. 3, pp. 382–394, 2016.

[32] M. Chen and G. A. Rincon-Mora, 'Accurate electrical battery model capable of predicting runtime and I-V performance', *IEEE Transactions on Energy Conversion*, vol. 21, no. 2, pp. 504–511, 2006.

[33] Q. Zhou *et al.*, 'Multi-step reinforcement learning for model-free predictive energy management of an electrified off-highway vehicle', 2020.

[34] Q. Zhou, Y. Zhang, Z. Li, J. Li, H. Xu, and O. Olatunbosun, 'Cyber-physical energy-saving control for hybrid aircraft-towing tractor based on online swarm intelligent programming', *IEEE Transactions on Industrial Informatics*, vol. 14, no. 9, pp. 4149–4158, 2017.

[35] G. Ma, M. Ghasemi, and X. Song, 'Integrated powertrain energy management and vehicle coordination for multiple connected hybrid electric vehicles', *IEEE Transactions on Vehicular Technology*, vol. 67, no. 4, pp. 2893–2899, 2017.

[36] T. Liu, X. Hu, S. E. Li, and D. Cao, 'Reinforcement Learning Optimized Look-Ahead Energy Management of a Parallel Hybrid Electric Vehicle', *IEEE/ASME Transactions on Mechatronics*, vol. 22, no. 4, pp. 1497–1507, 2017.

[37] S. M. Ahmeda and M. Abo-Zahhad, 'A new hybrid algorithm for ECG signal compression based on the wavelet transformation of the linearly predicted error', *Medical Engineering & Physics*, vol. 23, no. 2, pp. 117–126, 2001.

[38] H. L. MacLean and L. B. Lave, ‘Life cycle assessment of automobile/fuel options’, *Environmental Science & Technology*, vol. 37, no. 23, pp. 5445–5452, 2003.

[39] *CO2 emissions from fuel combustion 2018*. International Energy Agency (IEA), 2018.

[40] K. Deb and H. Jain, ‘An evolutionary many-objective optimization algorithm using reference-point-based nondominated sorting approach, part I: Solving problems with box constraints’, *IEEE Transactions on Evolutionary Computation*, vol. 18, no. 4, pp. 577–601, 2014.

[41] H. Jain and K. Deb, ‘An evolutionary many-objective optimization algorithm using reference-point based nondominated sorting approach, part II: Handling constraints and extending to an adaptive approach’, *IEEE Transactions on Evolutionary Computation*, vol. 18, no. 4, pp. 602–622, 2014.

[42] Q. Zhu *et al.*, ‘A novel adaptive hybrid crossover operator for multiobjective evolutionary algorithm’, *Information Sciences*, vol. 345, pp. 177–198, 2016.

[43] S. H. R. Pasandideh and Seyed Taghi Akhavan Niaki, ‘Multi-response simulation optimization using genetic algorithm within desirability function framework’, *Applied Mathematics & Computation*, vol. 175, no. 1, pp. 366–382, 2006.

[44] L. Li, X. Wang, and J. Song, ‘Fuel consumption optimization for smart hybrid electric vehicle during a car-following process’, *Mechanical Systems and Signal Processing*, vol. 87, pp. 17–29, 2017.